From automated MRI scan to finite elements

James Glimm[1], Hyunkyung Lim[1], Martin Bishop[2], and Soojin Kim[1]

[1] Stony Brook University, Stony Brook New York 11794, USA
[2] King's College, London, UK

Abstract. We present algorithms for the automated transition from scanned MRI images to finite element simulations. The algorithms are designed for the reconstruction of fine scale blood vessels as possibly important to defibrillation studies in electrocardiac physiology. The automated nature of the transition is essential for practical usage, as the otherwise necessary human intervention is prohibitive. The automated software relies on a mixture of public domain algorithms and new algorithms developed specifically for the current purpose. The problem of transitions from MRI images to accurate physiology is important in many medical applications, and much of our work will be helpful in more general cases. The definitive nature of the blood vessel problem which makes the entire analysis feasible is a conceptual model of the final geometry, as the connected branches of veins and arteries together with the inner and outer cardiac surface.

Keywords: MRI scan · defibrillation · cardiac blood vessels.

1 Introduction

Heart failure is a leading cause of death in the industrial world [1,2]. Understanding the normal and abnormal behaviors of the heart has been studied actively [11]. Ventricular fibrillation is a significant aspect of heart failure. It is fatal if not treated promptly, by an electrical shock to reset the cardiac conditions and to allow resumption of a normal heart beat. As an alternative to the traditional method of a single high voltage defibrillation shock, the method of Low Energy Action Potential (LEAP) [30] offers advantages, but details in its mode of operation remain to be clarified. The effectiveness of both LEAP and the strong shock method depend on localized discontinuities in the cardiac electrical conductivity to generate charges, known as virtual electrodes as a response to the electrical shock. These virtual electrodes interfere with the chaotic fibrillating state and bring about its termination, allowing resumption of a normal heart beat. The electrical discontinuities are located at the cardiac surfaces are of primary importance. The blood vessel walls are also a source of electrical discontinuity. They play a helpful but secondary role [4]. In a quantitative study of defibrillation [5], it was shown that both the shock strength and the minimum blood vessel size were important in determining which blood vessels were significant. Here a threshold of perhaps 50μ radius was identified. In [6], the interplay between

applied voltage and blood vessel diameter is examined, with most of the effect occurring at voltages larger than typical LEAP protocols or only for large blood vessels. Our aim here is to refine our understanding of this secondary role, especially as a function of the blood vessel size, and in a model of the full ventricle, beyond the thickened slab previously considered.

With high resolution 25μ MRI data of a rabbit ventricle, we have an opportunity to assess the roles of blood vessels of various sizes in the formation of virtual electrodes. This is where the automated analysis of this paper is important. Starting with the high resolution MRI data, we transition from segmentation (black-white stair step images) to finite element surface meshes to full volume finite elements meshes, to fiber orientation within the mesh to finite element fibrillation and defibrillation simulations. The main thrust of the present paper is the automated procedure, with the fibrillation and defibrillation studies not considered here. The automation is nearly complete, and remaining manual steps are sufficiently minor to allow systematic use of this technology. As the later stages of this suite of algorithms were developed in [7], our focus here is on the surface mesh and its construction from the segmented (stair steps) image.

In emphasizing an automated procedure, our goal is feasibility of the analysis. The decision to be made, fragment by fragment, is whether it is included in the analysis (radius above 50μ) or excluded from analysis. The number of such variables in the rabbit ventricle is of the order of tens of tens of thousands, and for a human heart, approximately $3^3 = 27$ larger, this number approaches million.

The human effort to manage the automated software is also a complicated and time consuming undertaking. Thus we allow instances where human judgement is less burdensome than the addition of a new software tool to the suite of analysis programs.

The governing equations for the electrical activity within the heart consist of a diffusion equation and a reaction source term depending on ionic currents. The equations and a finite element algorithm based on the CHASTE simulation platform (Cancer, Heart and Soft Tissue Environment) [8,9,10], for their solution are described in [7]. We solve the bidomain equations, representing the cardiac tissue at overlapping intracellular and extracellular domains [11], as is needed for the duration of the electrical shock. In the bidomain equations, a distinguished orientation within each mesh cell describes the direction of the fibers in that cell.

Computational resource requirements for this automated pipeline are a linux cluster or equivalent supercomputer access, both for computation and memory usage.

Finite elements are a form of discretization of the cardiac equations. In this technology, all of space is divided into tetrahedra, and the equations are solved on this basis, with the voltages defined as having values in each tetrahedra, As we use them here, they are adaptive, with the cardiac surfaces (inner and outer walls and blood vessels) lying on the boundary of the finite elements. With this framework, the surface mesh is the set of surface elements (triangles) that define the conductivity discontinuity boundaries (i.e. the heart walls and

the blood vessel (inner) surfaces). For some purposes, there are not one but two voltages defined in each cell, one representing the average of the voltages of the individual cardiac cells and the other the voltage on the average of the extracellular space. This is called a bidomain model, and is needed during the passage of the electrical shock as part of the defibrillation treatment. In the bidomain equations, the orientation of the cardiac fibers is important, and must be added to the equations to specify it. The standard bidomain equations for cardiac electro physiology [8] consist of a diffusion equation for the voltages (in the intra cellular and extracellular cardiac tissue and non cardiac tissue called bath) coupled to an ordinary differential equation for the ionic currents. The extracellular voltage and the bath voltage are solved as a single continuous potential, with no flux (Neumann) boundary conditions for the external bath boundary and a discontinuous diffusion tensor across the heart-bath boundary. The solution domain is denoted by $\Omega = H \cup B$, where H is the heart tissue and B is the bath. The boundaries of the heart tissue and bath are denoted by ∂H and ∂B respectively. The governing bidomain equations with the boundary conditions can be written as [33]

$$\chi(C_m \frac{\partial v}{\partial e} + I_{ion}(v, w)) - \nabla \cdot (D_i \nabla v) - \nabla \cdot (D_i \nabla v_e) = 0, \quad in\ H \tag{1}$$

$$\nabla \cdot (D_i \nabla v) + \nabla \cdot ((D_i + D_e) \nabla v_e) = 0, \quad in\ H \tag{2}$$

$$\frac{\partial w}{\partial t} + g(v, w) = 0, \quad in\ H \tag{3}$$

$$\nabla \cdot (D_b \nabla v_e) = 0, \quad in\ B \tag{4}$$

$$\mathbf{n} \cdot (D_i \nabla v) + n \cdot (D_i \nabla v_e) = 0, \quad on\ \partial H \tag{5}$$

$$n \cdot (D_e \nabla v_e) = n \cdot (D_b \nabla v_e), \quad on\ \partial H \tag{6}$$

$$n \cdot (D_e \nabla v_e) = I_e, \quad on\ \partial B \backslash \partial H \tag{7}$$

where χ is the surface to volume ratio of the membrane, C_m is the electrical capacitance of the cardiac tissue per unit area, I_{ion} is the ionic current over the membrane per unit area, which is calculated by the transmembrane potential v and the gate variable w. The gate function g and I_{ion} are determined by the cell ionic model, including the electroporation current I_{ep} [34,35,36]. The intra cellular and extracellular potentials and intra and extra conductivity tensors, denoted by v_i, v_e, D_i and D_e respectively, are defined in the heart tissue H. The extracellular potential is also defined in the bath B with the bath conductivity D_b. The unit normal vector at the cardiac surface, n, is oriented outward while I_e represents the electrical current across $\partial B \backslash \partial H$.

For both the surface and the volume mesh, mesh quality is important, of the numerical solution method will fail. Mesh quality is assessed in terms of approximate equal volumes of the mesh elements, areas of the surface mesh triangles and in both cases of the size of the vertex angles. The finite element equations are a linear system of equations, which cannot be solved explicitly. The solution is iterative and involves successive approximations. It is a general lore for such solutions that poor mesh quality makes the resulting iterative equations poorly conditioned. This means excessive computation time as the most favorable outcome, and more likely, failure of the iteration to converge. As there are many time steps and many such iterative solution steps, a high degree of reliability is essential, and this reliability requirement imposes a mesh quality condition.

The paper is organized as follows. The main thrust of the paper is contained in Sec. 2, where the automated algorithm is constructed. While many aspects of the algorithm can be used for the interpretation of a variety of MRI image data, we observe that its full force depends on high resolution data and on a clear conceptual understanding of the answer: an inner and an outer surface and connected branching networks of blood vessels (the veins and the arteries). Sec. 3 describes the ionic model of the equations and Sec. 4 contains a discussion of the model construction.

To complete the finite element equations in their bidomain form, we specify a fiber orientation in every mesh cell. This is constructed from an algorithm [12], as detailed experimental data is missing. We show a schematic diagram of the model construction for defibrillation studies in Fig. 1 and Fig. 2.

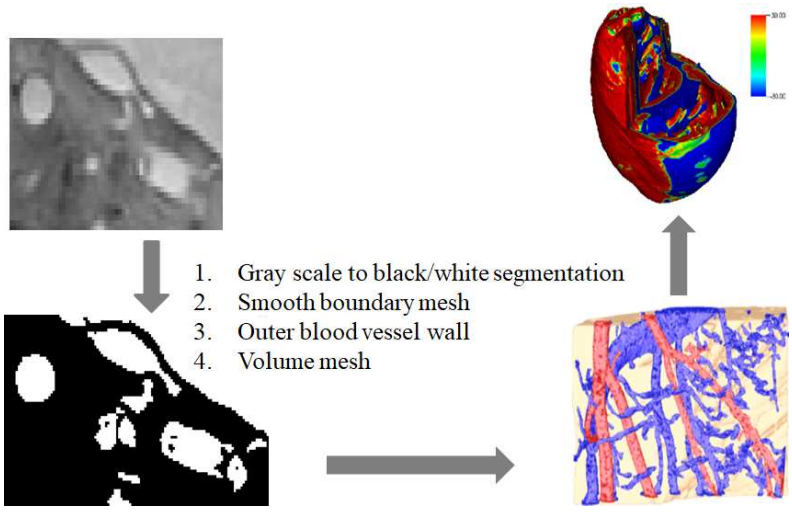

Fig. 1. Automated Construction of Whole Heart from MRI

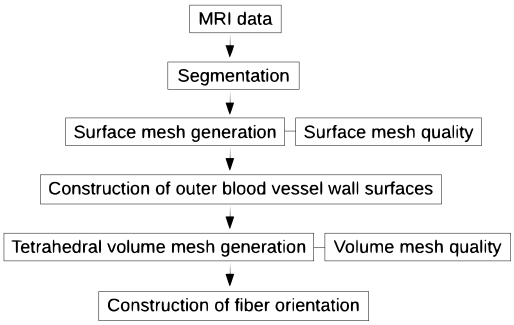

Fig. 2. A schematic diagram of the model construction for defibrillation studies.

2 The automated algorithm

We emphasize the large increase in automation achieved here vs. [5]. The [5] level of automation allowed detailed construction of a slice only from a rabbit ventricle. In contrast, we address detailed vascular resolution of the full ventricle with possible extension to the human ventricle.

Our approach is a combination of the use of existing tools and the skilled of new ones. Often, especially with our emphasis on public domain tools, their tools are immature and require additional effort to become useful. The tools are designed for use in a stand alone fashion, and these integration and interoperability is a further problem. As examples of new algorithms and developments, we mention several issues. Identification of which intermediate sized structure contain a segment of greater than 50 microns is not contained in any software package. The algorithm for growing the outer wall of a blood vessel from its inner wall, which are previously used in a hand corrected version is now fully automated [7]. The step of surface mesh quality was not previously considered, and we did not find a suitable public domain algorithm for [7].

2.1 Segmentation

The segmentation algorithm is described in detail in [6,13]. We only summarize a few of the highlights from this algorithm, which as given in these references is not fully automated. We only make use of the initial step of the method described in detail below. Our main trust is to by pass all but the initial step fully automated.

The methods of tissue preparation are described in detail in [6]. Initial segmentation only attempts to differentiate between tissue and non-tissue, with the further segmentation into distinct tissue classes (vessel walls vs. blood) accomplished later. In contrast to [13], the full resolution MR dataset was segmented, with no prior down-sampling. The heart of the method is an iterative use of level set technology, to identify a smooth surface separating distinct regions. Here the Insight Toolkit library, ITK, `www.itk.org` and several other software packages played an important role. A segmentation pipeline involving threshold, geodesic

and Laplacian level-set algorithms was employed in an automated manner, with specific parameter combinations for each filter obtained by visual inspection, as described in [13]. Following automated segmentation, due to poor MR contrast at some tissue boundaries, minor manual adjustments were needed throughout the dataset, again based on visual inspection.

For our present purposes, we take only the first pass segmentation version of the [6,13] segmentation protocol, which is fully automated. This algorithm leads to subsequent data problems which we address here.

2.2 Surface mesh

The surface mesh is constructed from the stair step segmented image of Sec. 2.1 by a level surface algorithm. The level surface algorithm finds an interpolating surface between the stair steps. At each point, its distance to the nearest black-white boundary is noted. This is a signed distance, and the 0 (mid) value of the interpolation is by definition the level surface. The level surface is triangulated via the marching cubes template based formula [14].

Blood vessel surface mesh data cleaning. The blood vessel surface mesh constructed in Sec. 2.2 can be divided topologically into distinct connected components (i.e. isolated fragments of the surface mesh). The decision variable is made for the component as a whole, to retain in the final model or to eliminate, on the basis of a size criteria. These components are the primary decision variables for subsequent analysis. There are 9642 of these components. The algorithm for the identification of the individual components is a marching front method, with the key decision criteria based on the fact that each triangle knows (has pointers to) each of the three triangles which it borders.

The mesh is of low quality. The many artifacts to be removed are mainly obvious to a human eye, but due to the large number of decision variables, an automated method is required. A fully resolved cardiac blood vessel model might have two components, one consisting of arteries and the other of veins, with possible exceptions due to the ventricle only nature of the data.

Our goal is to resolve only the blood vessels of radius 50μ or larger. Studies conducted by [6,13] indicated that a significant role for blood vessels of inner radius smaller than 50 microns appears to be excluded. These studies were conducted in idealized geometries. This conclusion appears to be accepted by most workers in this field. As the resolution is 25 microns, we divide the problem into three parts, large, intermediate and small sized components. The automated decision used to govern this separation is based on a count of the number of triangles in each component. The border between the sizes is adjusted by visual inspection. The large ones are components which are to be retained, the small ones are ones to be eliminated and the intermediate ones require a more careful analysis. The point of this division is to reduce the number of intermediate components as their detailed analysis is more expensive. Of the 9642 total components, we find 8246 small components and 142 large ones, leaving 1250

intermediate ones, about 15% of the total number of components. By numbers of surface triangles, the proportions is quite different, with 33,053,937 surface triangles assigned as 208,41,658 (about 2/3)to the large components, 7,467,308 (about 1/5) to the intermediate and 4,744,971 (about 1/7) to the small components.

Large components.

We search among the blood vessels for regions with a large volume. These are located within the large blood vessels. This search depends on the software package meshlab, `http://www.meshlab.net/`. Its use is manual, but not onerous in difficulty, as it is used to determine the full connected component of the blood vessels after manual identification of a large blood region starting point, with a relatively modest number of manual choices made. This algorithm brings along with the large starting blood vessel the many smaller ones branching off of it. The triangles identified in this manner are a preponderance of the total triangles of the surface. In Fig. 3 we show the five largest components identified in this manner.

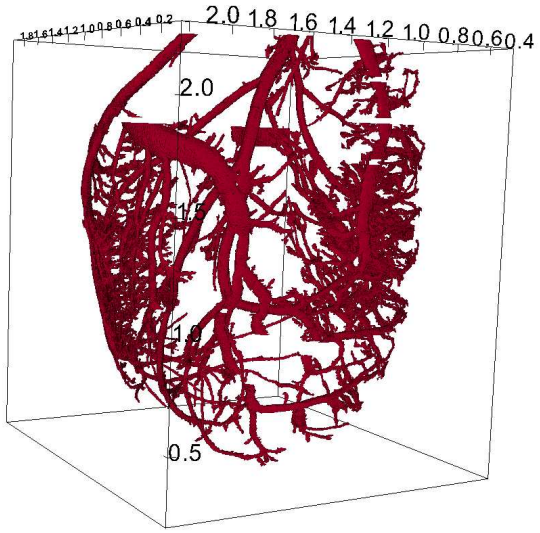

Fig. 3. We display the five largest blood vessel connected component networks. Each is identified starting from a large volume branching point and with the aid of a visualization tool finding all multiple smaller blood vessels connected to it. The units on the coordinate axes are in cm.

Intermediate components.

The most difficult case is the intermediate one. An example is shown in Fig 4. By adjustment of parameters, we place most of the components into the large

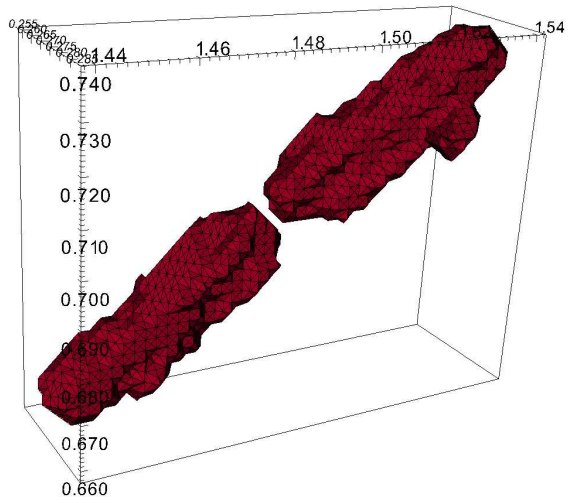

Fig. 4. We show an example of the intermediate sized blood vessel with two components. The components could be joined, but this seems to be a minor change in terms of surface triangles involved, which is where the virtual electrodes are located. Units in cm. on the coordinate axis indicate a radius of 100μ, indicating that these components are to be retained in the final model.

or small categories. The remaining intermediate sized components represent in blood vessels of a marginal size, near the 50μ radius criteria for elimination. We consider 1254 components of this category, a reduction 15% from the total number of components. Because of the borderline nature of the intermediate cases, these cases require a more careful and detailed analysis.

The detail analysis is based on the medial axis algorithm, is available from Matlab under the program name Skeleton3D. Public domain medial axis software is available from

`http://www.ams.sunysb.edu/~lindquis/3dma/3dma_rock/3dma_rock.html`

with technical description in [15]. The medial axis finds a precisely defined centerline for any component. It may have multiple branching points. We apply it only away from its branching points. As such, the medial axis defines a centerline of an extended 1D object. We form a normal plane to the centerline and

intersect the blood vessel surface with this normal plane. The result is a curve in the normal plane, changing as one moves along the medial axis. This curve, if approximated by an ellipse, has a major and a minor radius. The major radius is of interest here. If anywhere along the medial axis, the maximum radius exceeds 50μ , then (at least this fragment of) the component is to be retained.

The medial axis technology also offers the opportunity to join disconnected components, as the two components in question will appear as gaps in a single line or curve. We expect for the current purposes, this step will not be important, as the blood vessels joined in this manner will often be below the threshold of (50μ) radius. See Fig. 4. The medial axis (not shown in the figure) runs down the centerline of the two segments. Direct determination of the maximum radius within a component is also possible, avoiding use of the medial axis.

Small components.

The small components (which we might refer to as "fly specks") are regarded as segmentation artifacts and are removed from further analysis. Some of these represent small but under resolved blood vessels and that a more accurate reconstruction would "connect the dots" to yield an intact blood vessel. If this level of data analysis were achieved, the reconstructed blood vessels would be mainly below our target threshold, and after this careful reconstruction, would be removed from the analysis.

The number of components within the small category is 8246, by far a large fraction of the total number of components. Thus we see that the fly specks algorithm is a crucial first step in reducing the human complexity of the algorithm.

We show typical "fly specks" in Figs 5 and 6

Surface mesh quality Next we eliminate edges too small or too large. The large/small edge elimination is through a queue of large and small edges. The small edges are collapsed to a point, thereby reducing two triangles with this common edge to become edges themselves. Similarly, the edges too large are bisected by the insertion of a new point at the edge midpoint, thereby replacing two triangles having a common edge with four triangles having two common edges. These two operations are the inverse of one another, and in combination, will keep the side length ratios between triangles or within a single triangle within the range $[0.5, 2]$. Thus bad aspect ratios are also eliminated. The algorithm is similar to the volume mesh quality algorithm, previously described [7], so we omit further details.

Surface mesh verification The first check for surface quality is to ensure that the surface has no non-manifold edge. These are edges which border three or more triangles. The non-manifold search is automated, but repair is manual. An absence of holes in the cardiac surfaces is ensured by the same marching front algorithm discussed above.

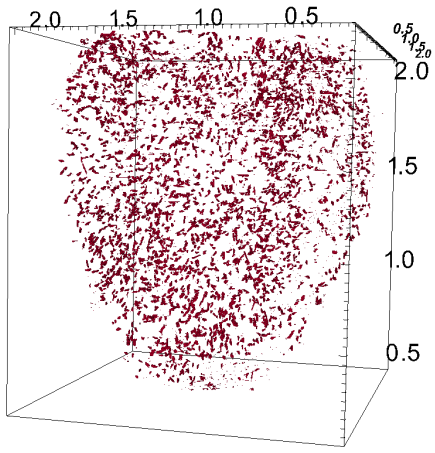

Fig. 5. The totality of all small components shows only low levels of coherent structure, and is regarded as "noise" in the present context. Units in cm.

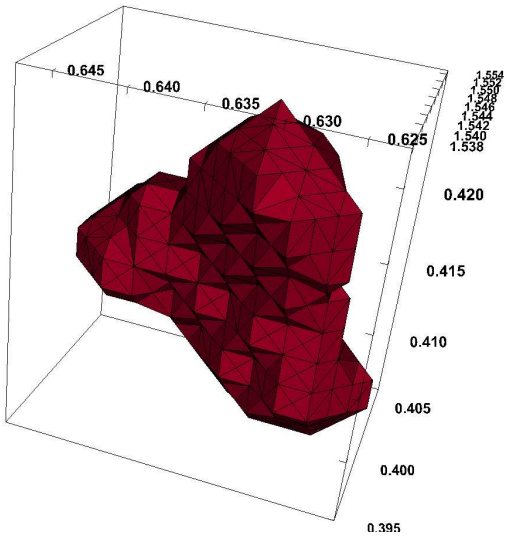

Fig. 6. A typical small component is shown.

We require that the entire cardiac surface consists of inner and outer wall, each without gaps and multiple fragments of artery and vein networks. Nonmanifold segments have been removed.

2.3 Vessel wall thickness

The segmentation yields the inner wall of the blood vessel only. Experimental correlations establish a vessel wall thickness according to its diameter and whether it is a vein or an artery. For the 142 large components, the distinction is based on expert knowledge.

As discussed in [7], the outer blood vessel wall surface is constructed as the solution of a dynamic equation

$$\frac{dx(t)}{dt} = -\mathbf{n} \tag{8}$$

to "grow" the inner surface in the direction $-\mathbf{n}$. The $\mathbf{n}$ is oriented outward relative to the cardiac tissue and so $-\mathbf{n}$ is outward relative to the blood vessel. $x(0)$ is some node of a triangle on the inner blood vessel wall, as initial conditions for (8), and the final time for this equation is set by the wall thickness. The dynamics of (8) are stable for outward growth of convex surface which is the normal case for the construction of the outer blood vessel wall from the inner wall. At branching points, where the veins divide, the inner surface is concave and the outward dynamics is unstable. Conceptually, consider a closed polygon in 2D to be propagated inward. If some of the vertex angles are sharp as with an elongated diamond shape, the points on the short axis can self intersect under inward propagation with a finite step size. Locations generating self intersections are characterized sharp surface angles and vertices or small triangles. The self intersections are resolved incrementally within the algorithm. If the local surface is concave, the stable version of this algorithm forces the outward growing surface to be single valued in infinitesimal steps.

2.4 Volume mesh

The public domain algorithm TetGen will construct a volume mesh which respects a given surface mesh [16]. However the mesh quality can be poor and the resulting discretized equations cannot be solved by the finite element method. Our mesh quality improvement algorithm was discussed in [7]. To improve the mesh quality, we make a list of problem mesh volume elements, and introduce an algorithm which will improve the local mesh in each of the several cases.

As with the surface mesh quality algorithm, the volume mesh quality is based on a queue of bad element edges. The bad edges are either too large or too small, and are eliminated by addition of a midpoint with two new triangle facets of four new tetrahedrons or the inverse operation, by collapse of an edge, combining two facing facets into an edge and four tetrahedrons into a single tetrahedron. As in the case of the edge mesh quality algorithm, the resulting edge ratios are

consistent within a factor of 2. Because this edge ratio criterion has already been enforced for the surface mesh, the volume mesh will never divide an edge which is part of the surface mesh. Thus the surface mesh is not modified as part of the volume mesh quality algorithm.

2.5 Fiber orientation

At least during the application of the shock, a bidomain conductivity model is needed, in which the electrical currents occur simultaneously within the fibers defining the cardiac cells and in the extracellular space that surrounds the fibers. The fibers are much finer that any feasible mesh resolution, so that within any mesh cell, both regions will occur. The resulting diffusion tensor then has distinguished properties along a single direction (the fiber direction). Thus

to complete the specification of the equations, the fiber orientation must be specified in every mesh cell. The limited experimental data for the fibers will establish general properties of the fiber orientation, but not its cell by cell orientation. Thus a software model, informed by the limited experimental data, is used to fill in the required fiber orientation at the mesh cell level [17]. The wrapping of fibers around and not terminating at blood vessels is discussed in [12].

3 Ionic model

A number of models of the ionic currents have been proposed at differing levels of completeness and complexity [18,19]. The canine ventricular cell model of Flaim et al. [20] includes as many as 87 variables, the Bondarenko et al. model [21] involves more that 100 variables. Although these complex models reproduce existing experimental results through careful selection of parameters, high parameter numbers often affect model robustness and introduce inconsistencies between models of the same animal species and specific regions of the heart [22], not to mention their computational expenses. Several reduced models have been proposed [23,24,25,23,26]. In the Fenton-Karma (FK) model [25],

$$I_{\text{ion}}(\phi, \mathbf{y}) = I_{\text{fi}}(\phi, v) + I_{\text{so}}(\phi) + I_{\text{si}}(\phi, w), \tag{9}$$

where I_{fi}, I_{so} and I_{si} denote the fast-inward, slow-outward, and slow-inward ionic currents respectively, and $\mathbf{y} = (v, w)$ is the vector of gate variables controlling the fast- and slow-inward components. The FK three-variable model is widely used, due to its capability to maintain most of the quantitative properties of the more complicated models, while reducing the computational complexity significantly [18]. These properties have made the FK model popular in a wide range of studies, including vortex dynamics in the myocardium [25], mechanisms for discordant alternate [27], temperature effects [28,29] and the promising field of low-energy defibrillation [30,31]. These models and the more complicated Mahajan model [32], which has been calibrated to experimental data for the rabbit,

are known not to allow a sustained fibrillation state. For this reason, following [4], we introduce an enhanced CA^{++} channel, with a parameter denoted R into into the model [32], which is believed to allow sustained fibrillation and a more accurate model of defibrillation.

4 Discussion

A combination of publicly available software tools with new algorithms described here and in [7] allow the construction of a detailed cardio-vascular mesh and finite element software model. The main point of the construction is to avoid prohibitive levels of human involvement in the construction. For this purpose, manual aspects of the construction are kept to a minimum.

The detailed mesh allows definitive studies of the importance (or not) of small features in the LEAP defibrillation protocol. The current data is for a rabbit. The authors believe that the same methods allow finite element models of a human heart, based on high resolution MRI data.

The optimal balance between efforts assigned to the various software stages remains to be explored. For example, automated but stronger segmentation algorithms appear to be a possibility.

5 Acknowledgements

This work is supported in part by the National Science Foundation grant NSF CPS-1446832.

References

1. Centers for Disease Control and Prevention. State-specific mortality from sudden cardiac death–united states, 1999. *MMWR. Morbidity and Mortality Weekly Report*, 51(6):123–123, 2002.
2. Elizabeth M. Cherry, Flavio H. Fenton, and Robert F. Gilmour. Mechanisms of ventricular arrhythmias: A dynamical systems-based perspective. *American Journal of Physiology-Heart and Circulatory Physiology*, 302(12):2451–2463, 2012.
3. R. H. Clayton, Olivier Bernus, E. M. Cherry, Hans Dierckx, F. H. Fenton, L. Mirabella, A. V. Panfilov, F. B. Sachse, G. Seemann, and H. Zhang. Models of cardiac tissue electrophysiology: Progress, challenges and open questions. *Progress in Biophysics and Molecular Biology*, 104(1):22–48, 2011.
4. Martin Bishop and Gernot Plank. The role of fine-scale atonomical structure in the dynamics of reentry in computational models of the rabbit ventricles. *J. Physiol.*, 18:4515–4535, 2012.
5. Martin J. Bishop, Gernot Plank, and Edward Vigmond. Investigating the role of coronary vasculature in the mechanisms of defibrillation. *Circulation: Arrthymia and Electrophysiology*, 5(1):210–219, 2012.
6. M. Bishop, P. M. Boyle, G. Plank, D. G. Walsh, and E Vigmond. Modeling the role of the cornary vasclature during external field simulation. *IEEE Transactions on Biomedical Engineering*, 10:2335–2345, 2010.

7. H. Lim, W. Cun, Y. Wang, R. Gray, and J. Glimm. The role of conductivity discontinuities in design of cardiac defibrillation. *Chaos*, 28:013106, 2018.
8. Gary R. Mirams, Christopher J. Arthurs, Miguel O. Bernabeu, and et al. Chaste: an open source c++ library for computational physiology and biology. *PLoS Computational Biology*, 9(3):e1002970, 2013.
9. Pras Pathmanathan and Richard A. Gray. Verification of computational models of cardiac electro-physiology. *Int. J. Numer. Methods Biomed. Eng.*, 30(5):525–544, 2014.
10. P. Pathmanathan, M.O. Bernabeu, R. Bordas, J. Cooper, A. Garny, J.M. Pitt-Francis, J.P. Whiteley and D.J. Gavaghan A numerical guide to the solution of the bidomain equations of cardiac electrophysiology. *Int. Prog. Biophys. Mol. Biol.*, 102(2–3):136–155, 2010.
11. R. H. Clayton, Olivier Bernus, E. M. Cherry, Hans Dierckx, F. H. Fenton, L. Mirabella, A. V. Panfilov, F. B. Sachse, G. Seemann and H. Zhang. Models of Cardiac Tissue Electrophysiology: Progress, Challenges and Open Questions. *Int. Progress in Biophysics and Molecular Biology*, 104(1):22–48, 2011.
12. M. Bishop, P. Boyle, G. Plank, and E. Vigmond. Modeling the role of coronary vasculature during external field stimulation. *IEEE Trans, Biomedical Eng.*, 57:2335–2345, 2010.
13. Martin J. Bishop, Gernot Plank, Rebecca A. B. Burton, Jrgen E. Schneider, David J. Gavaghan, and Peter Kohl Vicente Grau. Development of an anatomically detailed mri-derived rabbit ventricular model and assessment of its impact on simulations of electrophysiological function. *American Journal of Physiology - Heart and Circulatory Physiology*, 298(2):H699–H718, 2010.
14. W. E. Lorensen and H. E. Cline. Marching cubes: A high resolution 3D surface construction algorithm. *Computer Graphics*, 21(4):163–169, 1987.
15. W. B. Lindquist, S.-M. Lee, D. A. Coker, K. W. Jones, and P. Spanne. Medial axis analysis of void structure in three-dimensional tomographic images of porous media. *J. Geophys. Res.*, 101B:8297–8310, 1996.
16. Hang Si. Tetgen, a delaunay-based quality tetrahedral mesh generator. *ACM Transactions on Mathematical Software*, 41, 2015.
17. J. D. Bayer, R. C. Blake, G. Plank, and N. A. Trayanova. A novel rule-based algorithm for assigning myocardial fiber orientation to computational heart models. *Ann Biomed Eng.*, 40(10):2243–2254, 2012.
18. F. Fenton and E. Cherry. Models of cardiac cell. *Scholarpedia*, 3(8):1868–1868, 2008.
19. Catherine M. Lloyd, James R. Lawson, Peter J. Hunter, and Poul F. Nielsen. The CellML model repository. *Bioinformatics*, 24(18):2122–2123, 2008.
20. Sarah N. Flaim, Wayne R. Giles, and Andrew D. McCulloch. Contributions of sustained INa and IKv43 to transmural heterogeneity of early repolarization and arrhythmogenesis in canine left ventricular myocytes. *American Journal of Physiology-Heart and Circulatory Physiology*, 291(6):2617–2629, 2006.
21. Vladimir E. Bondarenko, Glenna C. L. Bett, and Randall L. Rasmusson. A model of graded calcium release and L-type Ca2+ channel inactivation in cardiac muscle. *American Journal of Physiology-Heart and Circulatory Physiology*, 286(3):1154–1169, 2004.
22. Elizabeth M. Cherry and Flavio H. Fenton. A tale of two dogs: Analyzing two models of canine ventricular electrophysiology. *American Journal of Physiology-Heart and Circulatory Physiology*, 292(1):43–55, 2007.
23. Colleen C. Mitchell and David G. Schaeffer. A two-current model for the dynamics of cardiac membrane. *Bulletin of Mathematical Biology*, 65(5):767–793, 2003.

24. G. Duckett and D. Barkley. Modeling the dynamics of cardiac action potential. *Physical review letters*, 85(4):884–884, 2000.
25. F. Fenton and A. Karma. Vortex dynamics in three-dimensional continuous myocardium with fiber rotation: Filament instability and fibrillation. *Chaos*, 8(1):20–47, 1998.
26. A. Karma. Electrical alternans and spiral wave breakup in cardiac tissue. *Chaos: An Interdisciplinary Journal of Nonlinear Science*, 4(3):461–472, 1994.
27. M. A. Watanabe, F. H. Fenton, S. J. Evans, H. M. Hastings, and A. Karma. Mechanisms for discordant alternans. *Computers & Fluids*, 12(2):196–206, 2001.
28. Flavio H. Fenton, Alessio Gizzi, Christian Cherubini, Nicola Pomella, and Simonetta Filippi. Role of temperature on nonlinear cardiac dynamics. *Physical Review E*, 87(4):042717, 2013.
29. Simonetta Filippi, Alessio Gizzi, Christian Cherubini, Stefan Luther, and Flavio H. Fenton. Mechanistic insights into hypothermic ventricular fibrillation: The role of temperature and tissue size. *Europace*, 16(3):424–434, 2014.
30. M. Chebbok, A. Squires, J. Schroeder-Schetelig, M. Zabel, G. Hasenfuss, E. Bodenschatz, F. Fenton, and S. Luther. Low-energy anti-fibrillation pacing (LEAP): A gentle, non traumatic defibrillation option. *European Heart Journal*, 33:381–381, 2012.
31. Flavio H. Fenton, Stefan Luther, Elizabeth M. Cherry, Niels F. Otani, Valentin Krinsky, Alain Pumir, Eberhard Bodenschatz, and Robert F. Gilmour. Termination of atrial fibrillation using pulsed low-energy far-field stimulation. *Circulation*, 120(6):467–476, 2009.
32. A. Mahajan, Y. Shiferaw, and D. Sato et al. A rabbit ventricular action potential model replicating ardiac dynamics at rapid heart rates. *Biophys J.*, 94:392–410, 2008.
33. Shuai Xue, Hyunkyung Lim, James Glimm, Flavio H. Fenton, and Elizabeth M. Cherry. Sharp boundary electrocardiac simulations. *SISC*, 38:B100–B117, 2016.
34. W. Krassowska. Effects of electroporation on transmembrane potential induced by defibrillation shocks. *Pacing and Clinical Electrophysiology*, 18:1644–1660, 1995.
35. D. K. Cheng, L. Tung, and E. A. Sobie. Nonuniform responses of transmembrane potential during electric field stimulation of single cardiac cells. *American Journal of Physiology - Heart and Circulatory Physiology*, 277:H351–H362, 1999.
36. Takashi Ashihara and Natalia A. Trayanova. Asymmetry in membrane responses to electric shocks: Insights from bidomain simulations. *Biophysical Journal*, 87:2271–2282, 2004.